Dynamic illumination of spatially restricted or large brain volumes via a single tapered optical fiber

Ferruccio Pisanello[#1,*], **Gil Mandelbaum**[#2], **Marco Pisanello**[1,4], **Ian A. Oldenburg**[2], **Leonardo Sileo**[1], **Jeffrey E. Markowitz**[2], **Ralph E. Peterson**[3], **Andrea Della Patria**[1], **Trevor M. Haynes**[2], **Mohamed S. Emara**[1,4], **Barbara Spagnolo**[1,4], **Sandeep Robert Datta**[3], **Massimo De Vittorio**[1,4], and **Bernardo L. Sabatini**[2,+]

[1]Istituto Italiano di Tecnologia (IIT), Center for Biomolecular Nanotechnologies, Via Barsanti, 73010 Arnesano Lecce, Italy

[2]Department of Neurobiology, Howard Hughes Medical Institute, Harvard Medical School, Boston, MA 02115, USA

[3]Department of Neurobiology, Harvard Medical School, Boston, MA 02115, USA

[4]Dipartimento di Ingegneria dell'Innovazione, Università del Salento, via per Monteroni, 73100 Lecce, Italy

[#] These authors contributed equally to this work.

Abstract

Optogenetics promises spatiotemporal precise control of neural processes using light. However, the spatial extent of illumination within the brain is difficult to control and cannot be adjusted using standard fiber optics. We demonstrate that optical fibers with tapered tips can be used to illuminate either spatially restricted or large brain volumes. Remotely adjusting the light input angle to the fiber varies the light-emitting portion of the taper over several millimeters without movement of the implant. We use this mode to activate dorsal versus ventral striatum of individual mice and reveal different effects of each manipulation on motor behavior. Conversely, injecting light over the full numerical aperture of the fiber results in light emission from the entire taper surface, achieving broader and more efficient optogenetic activation of neurons when compared to the standard flat-faced fiber stimulation. Thus, tapered fibers permit focal or broad illumination that can be precisely and dynamically matched to experimental needs.

*Correspondance: ferruccio.pisanello@iit.it. +Correspondance: bernardo_sabatini@hms.harvard.edu.

Conflict of interest
MDV, FP, BS, SD, and LS, authors on this study, are co-founders of Optogenix LLC, a company based in Italy that produces and markets the tapered fibers described here.

Data and code availability: All data and code are available from the authors.

Introduction

Optogenetic modulation of neuronal activity has become the dominant method of examining the behavioral consequences of activity in specific neuronal populations *in vivo*. This is due to the synergy of advances in two distinct but well-connected fields: the development of ever-improving light-activated modulators of electrical activity[1–3] and of technologies to deliver light within the brains of free-moving animals[4–8]. Nevertheless, attaining the full potential of optical neural control requires new technologies to better control the spatial extent of light delivery and more precisely match illumination to heterogeneous brain structures.

In certain applications, it is necessary to deliver uniform illumination to large brain areas, whereas for others confined illumination of small brain volumes is preferred. Ideally, both modes of illumination could be accomplished via a single, reconfigurable device. To this aim several approaches have been developed, including multiple implanted waveguides[8–10], multiple micro light delivery devices (μLEDs)[6,7,11,12], holographic illumination via head-mounted objectives[13] and multi-point emitting optical fibers (MPFs)[14,15]. However, these techniques have limitations: implanting multiple waveguides is highly invasive, μLEDs can heat tissue during prolonged illumination, and MPFs require higher input laser power to produce viable optogenetic control. Likely due to the difficulty and cost of building the required devices, these approaches have not been broadly utilized in neuroscience labs. Indeed, the most common light delivery method for optogenetic experiments remains flat-faced optical fibers (FFs), which deliver highly spatially heterogeneous illumination to a relatively small and fixed brain volume near the fiber facet. Furthermore, due to the relatively large and flat area of the cleaved end, these fibers can cause substantial tissue damage during insertion.

Here we describe a tapered optical fiber (TF) whose emission properties can be simply and dynamically reconfigured to switch between relatively homogenous light delivery to a large volume and spatially restricted illumination. Multiple wavelengths of light can be independently modulated and directed to subvolumes of interest. The device consists of a single, thin and sharp waveguide, thus minimizing invasiveness. To demonstrate the suitability of this approach for more uniform and efficient illumination of extended brain structures, experiments were performed in the primary motor cortex and striatum of awake head-restrained and freely moving mice. We demonstrate that by controlling the angle at which light is injected into the fiber, TFs can emit light from sub-portions of the taper to produce spatiotemporally resolved light patterns that subsample the volume of interest. We use this approach to achieve site specific optogenetic stimulation and demonstrate that activation of indirect pathway striatal projection neurons (iSPNs) in dorsal vs. ventral striatum has different effects on locomotion in freely moving mice while they explore an open arena. Thus TFs provide a simple, inexpensive, and easy to operate multipurpose system for optical control of neural activity.

Results

Design principles of tapered optical fibers

TFs are multimode fiber optics that have been engineered to taper gradually from their full width (125-225 μm) to ~500 nm. The taper angle is small ($2° < \psi < 8°$) such that the taper length varies between 1.5-5.6 mm (Fig. 1). This design was chosen to permit smooth insertion into the brain, reduce the implant cross-section, and expose a large area of the fiber for potential light emission. Ray-tracing and geometric models demonstrate the working principle of the device (Fig. 1a-b). A ray injected into the core of the fiber with an input angle θ is guided via total internal reflection (TIR) to the tapered region. At each reflection of the ray its propagation angle with respect to the fiber optical axis increases by an amount equal to the taper angle ψ (Fig. S1). This occurs until a critical section is met, at which TIR is lost and the ray radiates into the surrounding medium. Increasing θ increases the distance between this light-emission point and the taper tip (Fig. 1b) in a manner determined by the fiber numerical aperture (NA) and taper angle (Fig. S2 for optical fibers with NA 0.22 and 0.39 and $\psi=2.2°$ and $\psi=2.9°$, respectively). Therefore, the light input angle θ selects the output zone along the length of a specific taper.

A consequence of the dependence of the position of light emission on θ is that TFs can be used to emit light along the fiber in two fundamentally different ways. First, when light is injected into the TF using its full NA, light is emitted from a broad extent of the taper (Fig. 1c), as desired for illumination of spatially extended brain regions – e.g., the entire cortical thickness or the dorsal-ventral axis of the striatum. For a fiber of a particular NA, the length of the light-emitting segment (L) depends mainly on the taper angle. Ray tracing simulations indicate that L can be tailored from a few hundred micrometers up to a few millimeters in the case of 0.22 and 0.39 NA fibers with taper angles ψ ranging from 2.2° to 7.4° (Fig. S3).

We experimentally verified this effect in 0.22 and 0.39 NA fibers by immersing TFs in a fluorescein solution and imaging the resulting fluorescence distribution (Fig. S4). Decreasing the taper angle increases the length of the emitting segment to ~1 mm for 0.22 NA 50/125 μm core/cladding fibers and to ~2 mm for 0.39 NA 200/225 μm fibers (Fig. 1d). Thus, in this light-injection mode, a TF with the proper NA and taper angle can be chosen to match the linear extent of light output to the size of many mouse brain structures.

To compare the ray-tracing model with experimental results, we evaluated the emission length, referred to as $L_{0.5}$, over which the delivered intensity is more than 50% of its peak (Fig. S4). We found good agreement between modeling and experiments for both 0.39 NA and 0.22 NA fibers (Fig. 1d and Fig. S4). The differences observed at low ψ for 0.39 NA fibers arise because the taper is assumed to be linear in the ray-tracing model, whereas the real structure has a modest parabolic shape (Fig. S5). The diameter at which light starts to outcouple and the total light power delivered are nearly independent of the taper angle (Figs. S6). As a consequence, TFs with lower taper angles spread the available power over a larger taper surface (Fig. S7 and Fig. S8), potentially allowing light delivery to elongated brain regions.

Illumination of large brain volumes with TFs

Flat cleaved optical fibers (FFs) are commonly inserted just above a brain volume of interest and the delivered light is strongly attenuated by the tissue, allowing excitation of neurons located only up to a few hundred micrometers from the fiber end16–18. Significant excitation of more distant neurons requires large increases in laser power to overcome the approximately exponential decay in power density from the fiber face. In contrast, by virtue of their thin and sharp edge, TFs can be inserted into the volume of interest and light delivered along the length of the taper (Fig. 2). To evaluate the illumination pattern achieved in light-absorbing and scattering brain tissue, we implanted TFs and FFs into fluorescein-impregnated fixed mouse brain slices and imaged the fluorescence generated by light emitted from the fiber (Fig. 2a). As expected, FFs illuminate a small brain volume and fluorescence is strongly attenuated after a few hundred micrometers from the emitting flat-end facet (Fig. 2b). In contrast, TFs emit light along the taper length, resulting in elongated and more homogenous illumination of the tissue (Fig. 2c - d).

The differences in tissue illumination achieved by TF and FF arise from two important differences: (1) TFs emit light from a larger surface, i.e. the cone defined by L and ψ; (2) Light emerges from the TFs at a non-zero angle with respect to the taper axis (Fig. 1c). As a consequence, tissue absorption and scattering do not determine light distribution along the fiber axis as in FFs, but along the direction of emitted light, which has a significant component perpendicular to the taper axis. Notably, the depth of the excited volume can be tailored by selecting the fiber taper geometry and NA, instead of by increasing the laser power as commonly done in experiments with FFs. For instance, TFs with 0.22 NA and ψ=2.2° illuminate the whole cortical depth, whereas TFs with 0.39 NA and ψ=2.9° target most of the depth of the striatum (Fig. 2c-d).

In vivo examination of effective excitation in striatum, a large brain structure

To characterize the efficacy of TFs for *in vivo* optogenetics, we compared the ability of TFs and FFs to activate ChR2-expressing cells in striatum. Either a TF (0.39 NA and ψ=2.9°) or a FF (0.22 NA or 0.39 NA) was implanted in the striatum of adult transgenic mice (*Ador2a-Cre; Ai32*) expressing ChR2 in indirect striatal projection neurons (iSPNs) (Fig. 3). This mouse was selected for analysis because iSPNs are GABAergic neurons that locally inhibit other striatal neurons and inhibit recurrent excitatory inputs into striatum, minimizing secondary activation of cells not expressing ChR219. The TF was implanted at a depth of 3.7 mm and the FF at 2.3 mm, respectively. Light (473 nm, 1 mW outputted at fiber exit) was delivered at a 30 sec on/30 sec off cycle for 1 hour to awake animals in their home cages. To compare the spatial distribution of cells activated by light delivered through TFs and FFs, animals were euthanized 2 hours post stimulation and we performed fluorescence immunohistochemistry for c-fos, the protein product of an immediate early gene whose expression is regulated by neuronal activity20. C-fos was induced more uniformly across the ~2 mm dorsal-ventral extent of the striatum in TF- compared to FF-implanted animals (Fig. 3a-d). Furthermore, although light delivery through the TF stimulated cells throughout the dorsal-ventral axis (i.e. along the axis of the fiber), differential placement of the fiber permitted selective stimulation of either lateral or medial sub-regions of striatum (Fig. 3b). Thus, as suggested by the simulations and fluorescence excitation *ex vivo* (Figs. 1-2), TFs

deliver light *in vivo* across a spatially extended volume of tissue surrounding the thin fiber. Minimal c-fos was induced in animals that expressed ChR2 in iSPNs but were not stimulated and in wild type animals without ChR2 that did receive light stimulation (Fig. S9). Lastly, a clear advantage of TFs, likely resulting from their sub-micron sized tips, was the diminished tissue damage and activation of glia and microglia compared to FFs (Fig S10).

Optogenetic control of motor cortex with TFs

In order to examine the potential benefits of more uniform light delivery *in vivo*, TFs were tested in the primary motor cortex of awake head-restrained *VGAT-ChR2 BAC* adult mice[21], which express ChR2 in GABAergic neurons (Fig. 4a). A TF (NA 0.22, $\psi \sim 2.2°$) and FF were implanted serially near a 16-contact silicon multi-electrode array (Neuronexus). The FF was placed such that the face was at the same depth as the first emission point (shallow position) or the tip (deep position) of the TF. Light (473 nm) was delivered as 5 x 50 ms pulses at 5 Hz, repeated every 3s for 80 times. Output powers from the TF and FF were matched in order to examine the efficiency of each to inhibit cortex via stimulation of GABAergic interneurons. TFs more effectively suppressed cortical activity at lower power levels (Figs. 4b, S11): Inhibition with TFs was obtained at ~10 μW (~0.20 mW/mm^2, see Fig. S8 for estimated power density distribution along the taper) whereas FFs (NA=0.22) required ~5-fold higher powers to obtain a comparable effect at both depths (50 μW; ~25 mW/mm^2 http://web.stanford.edu/group/dlab/optogenetics/). Moreover, even at higher powers, inhibition is more pronounced with TFs, suggesting that tapered fibers stimulate a higher number of ChR2-expressing GABAergic neurons.

Dynamical selection of illuminated brain regions

A further benefit provided by TFs is the ability to dynamically control the illumination volume by changing the light entry angle θ at the input end of the fiber. The angle θ defines the subset of guided modes injected into the fiber[14,15] which in turn determines the cross-section of the taper at which light emits. The position of the emitting section along the taper depends on θ, as expected from the ray tracing simulations (Fig. S12; Movie 1). In particular, with low input angles light out-couples close to the taper tip, whereas light injected at high input angles is mainly emitted at sections farther from the tip.

To characterize the geometrical emission properties of TFs as a function of θ (Fig. 5) we implemented a simple optical path in which θ is changed by translating a mirror (Fig. S13a). Monitoring the fluorescence generated by a TF inserted into a fluorescein solution shows that the emitting segment (~300 μm long) can be moved almost continuously along ~1 mm or ~1.5 mm, respectively, in 0.22 NA/ψ=2.2° or 0.39 NA/ψ=2.9° TFs (Fig. 5a,b). Importantly, total delivered light power is nearly independent of θ, apart for input angles very close to the maximum acceptance angle (Fig. 5c). To rapidly scan the illumination across brain volumes we used a launching system with a scanning galvanometer and relay optics to change θ (Fig. S13b). This permits rapid switching between different emission segments (Movie 2) and near continuous movement of the emitting segment along the taper (Movie 3). Several launching paths can be combined to outcouple multiple wavelengths at the same time from independently addressable emission segments (Fig. S13; Movie 4).

To examine the suitability of this technique for restricted light delivery in brain tissue, site-selective light delivery as a function of θ was evaluated in fluorescein-stained acute mouse brain slices. Both 0.22 NA/ψ = 2.2° and 0.39 NA/ψ = 2.9° TFs allowed near-continuous tuning of the illuminated brain region in both cortex and striatum (Fig. 5d-g). Tissue absorption and scattering shorten the propagation of emitted light into the tissue, further constraining the spatial geometry of the illuminated area. This leads to spatially separated light delivery volumes, resulting in an easy-to-use and versatile method to direct the light stimulus along a ~2 mm segment by implanting a single fixed fiber.

In vivo multi-site stimulation

Selection of the emitting region of the taper is possible because different input angles generate different sets of guided modes in the fiber[15], which are out-coupled at different taper sections. However, while propagating into the fiber, subsets of guided modes may undergo modal mixing induced by fiber impurities and bends. This could redistribute part of the guided light power to other modes and rearrange light emission along the taper. To evaluate the viability of using TFs for site-selective light delivery in moving mice, we measured the effects of bending and shaking on TF light output (Fig. S14). For a fixed input angle (θ=17°), the patch fiber carrying light to a TF with 0.39 NA/ψ = 2.9° was shaken and bent while emission into a fluorescein droplet was recorded at high frame rate (~100 fps) (Movies 5-7). The fluctuations in fluorescence peak intensity, full-width at half maximum, and center were each less than 5% with fiber shaking and bending (Fig. S14).

To demonstrate the feasibility of multi-site optogenetic stimulation through a TF in an individual animal, TFs were designed (0.39 NA, ψ =2.3°) and implanted spanning the dorsal and ventral medial striatum of adult mice expressing ChR2 in iSPNs (*Ador2a-Cre; Ai32*). An optical pathway was designed (Fig. 6a) and calibrated to deliver a similar power density from the distal (ventral striatum) and proximal (dorsal striatum) sites (Fig. 6c) using, respectively, 8° (θ_1) and 22.5°(θ_2) launch angles (Fig. 6a; Fig. S15).

Eight days after implant surgery, mouse spontaneous locomotion was monitored in an open circular arena with depth time-of-flight cameras[22]. Light was delivered to the brain via an optical commutator, a lightweight patch cord (200 μm core, 0.39 NA, 1 meter long), and two fiber-fiber conjunctions as typically used for unrestrained mouse behavior experiments (Fig. 6a-b). The experimental paradigm consisted of 3 min blocks of either no stimulation (ns), or laser input to the fiber at angle 1 (θ_1) or angle 2 (θ_2) repeated in the following pattern: ns-θ_1-ns-θ_2-ns-θ_1-ns-θ_2-ns, corresponding to alternating stimulation of ventral (θ_1) and dorsal (θ_2) striatum separated by periods of no stimulation (Fig. 6c-d). On the subsequent day the order of ventral (θ_1) and dorsal (θ_2) stimulation were reversed such that 9 blocks per session were recorded in each of 2 days. Basic analyses of locomotion speed and orientation (Fig. 6e) reveal that stimulation at either dorsal or ventral striatum reduced locomotion and triggered contraversive spinning in individual mice (Fig. 6f), as expected for unilateral activation of iSPNs[23]. Ventral stimulation via light injection at angle θ_2 inducing more profound effects (distance traversed/3 min: ns: 3.16±1.45m, n=10 3 min blocks over 2 imaging days for 1 mouse; ventral (θ_1): 0.41±0.27, n=4/2/1 sessions/days/mouse; dorsal

(θ_2): 1.18±0.18, n=4/2/1 sessions/days/mouse; θ_1 vs. θ_2: p=0.0286. θ_1 vs. ns: p = 0.002; θ_2 vs. ns: p =0.002) (Fig. 6g).

To understand if dorsal vs. ventral stimulation had qualitatively different behavioral consequences, mouse locomotion and posture (Fig. 7a) were analyzed using a machine learning approach that automatically detects repeated time varying "syllables" corresponding to the animal's postural dynamics[22]. This technique produces a hidden Markov model in which each state encapsulates the postural dynamics of the mouse in each expressed behavioral syllable. The model is built using 3-dimensional information derived from video collected at 30 Hz for all mice across all imaging sessions and stimulation conditions. In this case, 14 syllables were sufficient to explain on ~94% of locomotion behavior in all sessions (ns: 87%; ventral (θ_1): 98%; dorsal (θ_2): 97%) (Fig. 7b).

Consistent with the previously described effects of iSPN stimulation on locomotion[23] and those revealed by simple video tracking (Fig. 6) the most strongly induced behavior during stimulation was "pausing" (% of time spent in syllables 1 and 2: ns: 1%; ventral (θ_1): 74%; dorsal (θ_2): 38%) corresponding to a motionless mouse (Fig. 7b and Movie 8). The expression of these pause syllables varied across conditions and was most prominent during ventral stimulation (Fig. 7b).

Movement related syllables (syllables 3-14) were also differentially expressed across stimulation condition (% of time spent in syllables 3-14: ns: 86%; ventral (θ_1): 24%; dorsal (θ_2): 59%) (Fig. 7b). Furthermore, specific movement-related syllables were more strongly induced by dorsal (e.g. 4,5,6) stimulation whereas others showed the converse pattern (e.g. 3,7) (Fig. 7c). Thus, these results are not consistent with ventral stimulation simply being more effective as discrete motor actions are evoked by stimulation at each site. Each differentially modulated syllable represents a consistent but distinct motor action: syllable 6, more strongly evoked by dorsal stimulation, involves the animal shaking its body left and right, whereas syllable 7 is a spin to the left (head moves left while tail moves right) (Fig. 7d and Movies 9 and 10). Importantly, the head and tail trajectories are similar during epochs of stimulation of the dorsal vs. ventral striatum despite their differences in expression frequency (Fig. 7c-d).

Discussion

We demonstrate that TFs have several advantages for light delivery in the brain that might allow this tool to replace the flat-cleaved optical fibers that are typically used for optogenetic experiments. First, TFs are multipurpose such that the same device allows either large-volume or site-selective light delivery. Second, by virtue of their tapered and smaller average cross section, TFs are minimally invasive and can be implanted directly into the brain region of interest. Third, they are simple to operate and compatible with optical equipment commonly present in neuroscience labs employing optogenetics.

Illumination of large brain volumes

When used to deliver light from the entire taper surface, TFs overcome one of the principal difficulties facing experiments in *in vivo* optogenetics – achieving uniform effective

illumination of large brain structures with minimal invasiveness and light power. Although effective stimulation of neuron cell bodies expressing ChR2 can be obtained with power densities in the range 1-5 mW/mm^2 [24,25] (and sometimes <1 mW/mm^2, depending on the sensitivity of the ChR2-expressing cells)26, many published studies utilize orders of magnitude higher power16,27–29. This likely arises because the FF is often positioned above the brain nucleus of interest to minimize damage. Due to the exponential fall off in power density from the FF, this necessitates the use of high light powers in order to stimulate cells throughout the nucleus16,17,30 and can result in local tissue heating in the range of several degrees18. By both permitting insertion of the fiber into the nucleus of interest and by delivering light along the linear extent of the taper, TFs achieve efficient light stimulation. This feature may be even more important when considering inhibitory and spectrally shifted opsins that may require more light to achieve effective neuronal perturbation.

Large brain area illumination with TFs is easily achieved with standard fiber-coupled lasers or LEDs, including with inexpensive LED-based commercial fiber launch systems (Fig. S15) that naturally inject light over a large NA and produce emission over the fiber face. Furthermore, the approach is viable for chronic use in freely moving tethered mice and for acute insertion in head-fixed mice.

Spatially restricted and dynamically controlled light delivery

TFs also solve the problem of achieving on-the-fly adjustable light delivery, even of multiple light wavelengths, to sub-volumes of brain tissue (Movies 1-4; Fig. 5-7). Site-selective light delivery is achieved using a simple optical setup that injects light into the fiber with a defined and adjustable angle θ. At the minimum, this setup consists of one lens and one translating mirror for slowly adjusting θ (Fig. S13a). For high-speed control, three lenses and one galvanometric mirror (Fig. S13b) are used to change θ quickly. With this approach, the emitting region can be modified step-by-step (every 20 ms in Movie 2) or continuously at various speeds (Movie 3).

Previous use of tapered fibers

Although the ability of TFs to provide uniform as well as dynamically controlled restricted illumination has not been previously recognized, sharpened fibers have been sporadically used to increase light delivery angle, to reduce invasiveness, and for biological discovery31–33. This prior work exploits chemical etching of fibers34, which can produce steep tapers of short lengths and has not been demonstrated to be able to make long, gradual, and tightly controlled tapers needed to illuminate large brain structures. In contrast, we pull the fibers rapidly after heating by lasers with very small taper angles, and demonstrate reproducible fabrication of fibers with customized taper length and angle. Previous use of chemically etched fibers appears to have been to minimize tissue damage31,33 and provide a broader illumination angle from the tip33. These studies may draw inspiration from previous work32 in which chemically etched fibers were attached to tetrodes to generate arrays of "optrodes" capable of both photostimulation and recording neural activity. In this study light emission appears to be only from the taper tip and results in a broader illumination angle (their Figure 1B and Figure 3). It is unclear in these studies if light was injected at the fiber back aperture

using its full NA, as necessary to achieve light output from the entire fiber face. As far as we know, no previous study demonstrates, as is done here, scanning output along the taper length (Fig. 5) and its application in freely moving animals (Fig. 6-7).

In addition, coating TFs with metal with small openings restricts light delivery. Lambelet et al used TFs covered with aluminum to restrict light emission and collection to a ~100 nm fiber tip, as needed for near-field fluorescence 34. We previously restricted light emission from a fiber by coating it in gold and making small holes in the metal coat14. These metalized and milled fibers were handed-crafted, requiring hours of work by an individual at a highly specialized machine that combines focused ion beam milling within a scanning electron microscope and resulting in ~$1000/fiber production costs. Furthermore, they could not be used for large volume illumination and provided unidirectional illumination at fixed, predefined spots whereas the new technology allows continuous and dynamic selection of illumination zones at a low cost.

Novel classes of optogenetic experiment for biological discovery

From the perspective of an experimental neuroscientist, several classes of experiments become possible by exploiting the flexible and controllable nature of light delivery with TFs. For example, subregions of the striatum subserve different functions with specialized contributions to behavior being evident along the dorsal/ventral as well as medial/lateral axes and course topographic mapping to cortex laid out along the anterior/posterior axis35. This suborganization is not possible to access in a single experimental animal. As we demonstrate (Fig. 3,6-7), with a TF it is possible to illuminate an elongated column of striatum that spans the dorsal/ventral axis and compare, in a single animal, the effects of selective optogenetic manipulation of subregions along the fiber axis. Given that the striatum spans several millimeters in the mouse, these experiments are impractical with standard FFs as these can neither deliver light to the entire structure nor be repositioned for selective stimulation. Furthermore, with extended TFs a single fiber can be inserted to deliver light to both cortex and striatum. Since light of different wavelengths can be out-coupled from different zones and independently controlled (Movie 4), it will be possible to examine the effects of interactions between areas. For example, one can examine if the motor effects of inhibition of motor cortex can be overcome by excitation of the striatum.

In addition, as optogenetics becomes accessible in primates36, the larger brain structure will require the use of TFs for effective perturbations. For example, visual cortex of macaque is several millimeters in thickness with different cellular and receptive field properties in different layers37. In this classic experimental system, current light delivery devices are unable to manipulate cells throughout all layers or, through a single device, test the effects of manipulations of superficial versus deep layer neurons. Furthermore, given the tight topographic organization of primate visual cortex and the use of individual animals for many recording sessions, it is valuable to have a device such as a TF with gentle taper for multiple insertions in each recording sessions.

In summary, we exploit TFs with small taper angles to achieve near uniform illumination of extended brain structures as well as to sample subregions of interest along a taper segment up to 2 mm while causing significantly less damage to the brain compared to FFs. The

devices were tested in both mouse motor cortex and striatum, showing ~5 times lower excitation power threshold and larger excitation volume, compared to flat faced fibers. Furthermore, we demonstrate their effective use through optical commutators and patch cords to compare the effects of stimulation of dorsal vs. ventral striatum in individual unrestrained mice spontaneously exploring an arena. Coupled to the minimum invasiveness of the device, the simplicity of the technique and its intrinsic compatibility with both laser and LED sources, we suggest that this approach can greatly complement existing methods for light delivery in optogenetics experiments and has the potential to replace commonly used flat-faced fibers for many applications.

Methods

All mouse handling and manipulations were performed in accordance with protocols approved by the Harvard Standing Committee on Animal Care following guidelines described in the US National Institutes of Health Guide for the Care and Use of Laboratory Animals. In this study we used both male and female mice (P>60). We used the *VGAT-ChR2* mouse from the Jackson Laboratory (B6.Cg-Tg(Slc32a1 COP4*H134R/EYFP) 8Gfng/J, stock #014548), the *Ador2a-Cre* mouse line from GENSAT: (B6.FVB(Cg)-Tg (Adora2acre) KG139Gsat/Mmucd) crossed to *Ai32* mouse line from Jackson Laboratory (RCL1-ChR2(H134R)/EYFP, stock #012569). In addition we used C57BL mice from Charles River (C57BL/6NCrl, stock #027).

Ray tracing simulations

The commercial optical ray tracing software Zemax-OpticStudio (http://www.zemax.com/) was used to design and simulate the performances of TFs. The single TF was modeled as a straight core/cladding segment followed by a conical taper. The materials forming all the components of the TFs and the surrounding media were assumed homogenous (refractive index constant in space). The core/cladding diameters are 50/125μm and 200/225μm for fibers with numerical aperture NA=0.22 and NA=0.39, respectively. core/cladding refractive indexes were set as specified by the fiber producer: 1.464/1.447 for *NA*=0.22 and 1.464/1.411 for NA=0.39. Since the tapers were obtained by heat and pull, commonly resulting in a melting of core and cladding materials in the tapered regions, taper refractive index was assumed as the average of core and cladding refractive indexes weighted to the core and cladding cross sectional areas. This resulted in tapers refractive index of 1.450 for fibers with NA=0.22 and 1.453 for fibers with NA=0.39. The length of the core/cladding block was set to 4mm, whereas the length of the taper is a function of the taper angle.

For results of simulations reported in Fig. 1b and Fig. S2, the source was modeled as a single ray injected into the fiber with a defined angle of incidence with respect to fiber optical axis. For simulations reported in Fig. 1 and Fig. S3 and S4 a monochromatic source (λ=473 nm) was modeled as a bundle of unpolarized parallel rays having a Gaussian intensity profile. The source was focused into the core/cladding section of the fiber through a Zemax model of the experimentally used aspheric condenser (Rochester Precision Optics www.rpoptics.com). Model A-375-A with focal length f=7.49 mm, NA=0.29, clear aperture of 4.50 mm was used for TFs with NA=0.22 (input Gaussian beam radius 1.66 mm

measured at $1/e^2$, resulting in a focused waist of 1.6 μm RMS spot radius), whereas model A-390-A with f=4.60 mm, NA=0.47 and clear aperture of 4.90 mm was used for fibers with NA=0.39 (input Gaussian beam radius 1.84 mm measured at $1/e^2$, resulting in a focused spot of 1.9 μm RMS spot radius). The former coupler was used only with the NA=0.22 optical fiber, with a Gaussian beam radius of 1.66 mm which focuses on the fiber core with a 1.6 μm RMS spot radius; the latter was used with both fibers, with a Gaussian beam radius of 1.84 mm which produces a 1.9 μm RMS spot radius. For simulations displayed in Fig. S12 a parallel and unpolarized Gaussian beam with radius 25 μm at $1/e^2$ intensity was injected at different input angles.

The irradiance profile of the light outcoupled from the taper was recorded through a rectangular pixelated detector laid along the taper sidewall (Figure S4). Detector length was set as the taper side length and its width to 20 μm. These profiles are then averaged along the short side of the detector and fitted with a Gaussian function. The full-width at half maximum criterion was used to retrieve the emission length ($L_{0.5}$, measured axially from the taper tip) from the irradiance profiles. For each single ray tracing session, 5M rays were launched into the system and each ray was split at the boundary between two different media, according to Fresnel coefficients.

Ray tracing is appropriate for the modeling shown in Figs. 1, S2-4. Mode theory (Helmholtz equation38) is typically employed for an accurate analysis of light propagation. This is particularly important when the waveguide size is comparable to the wavelength of light. In our tapered fiber this condition applies only close to the fiber tip. We describe the working principles of TFs using ray optics because the main effects we exploit are not taking place at the tip, but rather over the whole extent of the tapered fiber, and mostly at fiber diameters well above a few micrometers. Ray tracing is used to characterize the full-NA injection method, with good agreement with experimental results (Fig. 1d). In the section "In vivo multisite stimulation" we describe the working principle of the device based on selective modal out-coupling along the taper.

TFs stub preparation and optical measurements

Tapered optical fibers with taper angles in the rage $2° < \psi < 8°$ were obtained from OptogeniX (www.optogenix.com) and connected to a ceramic ferrules following the procedure described previously39. A ceramic ferrule-SMA patch cable was used to connect the fiber stub to the optical setup displayed in Fig. S4 for full NA light injection or to the setups schematized in Fig. S13 for site-selective light delivery. The taper was immersed into a fluorescent PBS:fluorescein solution or inserted in stained brain slices positioned under a 5X objective of a fluorescence Zeiss microscope equipped with a FITC filter. Images were acquired with a Hamamatsu Orca Flash 4.0. sCMOS camera at a resolution 2048x2048 pixel (pixel depth 16 bit). Optical output power was measured in air. In the case of the multiwavelength experiment reported in Movie 4, the taper was immersed into a drop of diluted milk to induce scattering of outcoupled light and detected with a color CCD camera.

For imaging light delivery geometry in fixed brain slices, slices of thickness ranging from 200 μm to 400 μm were permeabilized with Triton X-100 0.1% for 10 min to allow homogenous cell staining through the whole brain slice thickness and then washed with 1X

PBS three times. Slices were then incubated with Sybr Green 1:10.000 (Thermo Fischer Scientific Inc.) for 20 min on an orbital shaker in dark and thoroughly washed with 1X PBS.

Analysis of c-fos induction

Transgenic adult (*Ador2a-Cre; Ai32*) animals (P>60) were anesthetized with isoflurane and placed in a small animal stereotaxic frame (David Kopf instruments). Under aseptic conditions, the skull was exposed and a small hole was drilled. Animals received 0.01mg/gram of sterile Ketofen (Zoetis). For FF implanted animals and the lateral striatum TF implanted animal the hole was made at 0.85mm anterior, 1.95mm lateral from bregma. For the medial striatum TF implanted animals the hole was made at 0.85mm anterior, 1.65mm lateral from bregma. A TF (3.7mm from pia) or FF (2.3 mm from pia) was inserted manually using a cannula holder (David Kopf instruments). The TF or FF was then glued in place (454 instant adhesive, Loctite). And the skull was covered with dental cement (CandB Metabond, Parkell inc). Regardless of the implant-surgery time animals were under isoflurane anesthesia for a total of 1 hour before stimulation started. Stimulation was delivered in 30-second on/off cycles for a total of 1 hour (473 nm, 1 mW outputted at fiber exit). 2 hours post stimulation animals were euthanized with 0.2 ml of 10% Fatal Plus solution (Vortech pharmaceuticals) in saline before being perfused with 4% paraformaldehyde (PFA) in 0.1M sodium phosphate buffer (PBS). Brains were post fixed for 24 hours in PFA, washed in PBS, and sectioned (50um) coronally.

Immunohistochemistry conditions were the same for all animals. In short, slices were incubated in PBS blocking solution containing 0.3% TritonX (PBST) for 1 hour at RT. Slices were then incubated over night at 4°C in the same blocking solution with 1% goat serum and 1ug/ml c-Fos rabbit polyclonal IgG antibody (H-125, Santa Cruz Biotechnology). The next day slices were rinsed 3x10min in PBS before being incubated in the blocking solution with secondary antibody (1mg/ml goat anti-rabbit Alexa Fluor 647 or Alexa Fluor 594, Life Technologies). The slices were then rinsed again and mounted. After drying, slices were coverslipped with ProLong antifade mounting media containing DAPI (Molecular Probes) and imaged with an Olympus VS 120 slide-scanning microscope using a 10x objective.

Analysis of glial response to fiber insertion

The implant surgery was similar to the one described during the analysis of c-fos induction but both implants were positioned at 0.8mm anterior and 2.0mm lateral to bregma . In addition, the TF was implanted at a depth of 4.0 mm and the FF at 3.5mm. Adult (*C57BL/6NCrl*) animals (P>60) were euthanized 48 hours post-surgery and perfused as described above. To compare the spatial distribution of microglia and astrocytes activated near the implant, we performed fluorescence immunohistochemistry (as described in Analysis of c-fos induction section) for GFAP (primary rabbit anti-GFAP, Dako Z0334, 1:1000 dilution; secondary 1:1000 goat anti rabbit 555) and CD68 (primary rat anti-CD68, Biorad MCA1957; 1:200 dilution; secondary 1:1000 goat anti rat 647) respectively. 6 coronal sections surrounding the implant were imaged with a VS120 Olympus slide-scanning microscope. Quantification of fluorescence intensity was performed in ImageJ (NIH). ROIs of striatum were determined based on the Allen Brain Atlas 2004. For each section, the total

fluorescence intensity summed from the left and right hemispheres was normalized to one such that the fluorescence per hemisphere is expressed as a fraction of the total for that section. No comparisons were made between sections.

Multielectrode array recordings

Recordings in primary motor cortex of adult (*VGAT-ChR2*) animals (P>60) and off-line analysis of spiking rates were accomplished as previously described [19]. Mice were habituated to head-restraint prior to the recording session. Only one fiber optic (TF or FF) was inserted at a time and the effects of transient stimulation of cortical inhibitory neurons on identified units were examined. For each unit, spiking rates were normalized to the pre-illumination rate. Averages were calculated across neurons.

Open field surgery

The surgery for TF implant was as described above in the analysis of c-fos induction with coordinates for the TF in striatum being 0.85A, 1.4L, 4.1D. Adult (*Ador2a-Cre; Ai32*) animals (P>60) recovered for 5 days post surgery and were handled for 3 days before experimentation.

Behavior

On the day of the experiment animals were positioned in the open field arena. The experimental paradigm consisted of 3 min blocks of either no stimulation (ns), or laser input to the fiber at angle 1 (θ_1) or angle 2 (θ_2) repeated in the following pattern ns θ_1 ns θ_2 ns θ_1 ns θ_2 ns, corresponding to alternating stimulation of ventral (θ_1) and dorsal (θ_2) striatum separated by periods of no stimulation. On the subsequent day of analysis the order of ventral (θ_1) and dorsal (θ_2) stimulation were reversed.

Open field analysis

Mice were recorded using a Microsoft Kinect (v1), which records depth video data at 30 frames per second. For data in figure 6, scalar features were extracted using previously published methods[22]. For modeling data presented in Fig. 7, the open field behavior was analyzed using previously published methods[22]. In brief, the data were subjected to machine learning methods that describe the mouse's behavior as re-usable sub-second modules, or syllables. All free parameters were set to the values described in Wiltschko et al[22] with the exception of the stickiness parameter, kappa, which sets the model's tendency to remain in the same syllable over time (rather than switch between different syllables). This parameter was tuned so that the overall syllable duration distribution qualitatively matched a model-free analysis of behavioral change-points as in Wiltschko et al[22]. For this analysis we set kappa to 291,600. For head and tail positioning of the mouse in Fig. 7, the head and tail position were computed first by fitting an ellipse to the image of the mouse. The head and tail positions were defined as the two farthest points of the ellipse (i.e. the points of the ellipse that intersect with its principal axis).

Statistics

Statistical comparisons were performed in Prism (Graphpad) with non-parametric tests. For the data in Figure 6, a Mann-Whitney two-tailed U test was performed with n-values of 10, 4, and 4 for ns, θ_1 stimulation and θ_2 stimulation. For further details, please see the main text and Figure 6 legend. Each n represents one 3 minute imaging sessions with half the sessions collected on day one and half on day 2. Figure S11. For the data in Figure S11, a Kruskal Wallis ANOVA with Dunn's multiple comparison correction was performed and the n-values are 45, 49, 51, 51, 28, 28, 28, 28, 48, 49, 49, and 49 cells for 10, 50, 100, and 200 µW power for the TF, shallow FF, and deep FF. Please see Figure S11 legend for further details. Please see the reporting checklist for further details. No statistical methods were used to determine sample sizes *a priori*. The sample size was chosen based on prior experience with similar experiments. Normality was not assumed and no per sample calculation of variance was performed. No randomization or blind analysis was used. However, for Figure 6 the analysis was performed with automated routines with no user intervention and the stimuli were delivered in interleaved and counterbalanced orders. No criteria for data exclusion were used.

Supplementary Material

Refer to Web version on PubMed Central for supplementary material.

Acknowledgements

References

1. Dawydow A, et al. Channelrhodopsin-2–XXL, a powerful optogenetic tool for low-light applications. Proceedings of the National Academy of Sciences. 2014; 111:13972–13977.

2. Hochbaum DR, et al. All-optical electrophysiology in mammalian neurons using engineered microbial rhodopsins. Nat Meth. 2014; 11:825–833.

3. Govorunova EG, Sineshchekov OA, Janz R, Liu X, Spudich JL. Natural light-gated anion channels: A family of microbial rhodopsins for advanced optogenetics. Science. 2015; 349:647–650. [PubMed: 26113638]

4. Lee, J., Ozden, I., Song, Y-K., Nurmikko, AV. Nat Meth. advance online publication; 2015. Transparent intracortical microprobe array for simultaneous spatiotemporal optical stimulation and multichannel electrical recording.

5. Canales A, et al. Multifunctional fibers for simultaneous optical, electrical and chemical interrogation of neural circuits in vivo. Nat Biotech. 2015; 33:277–284.

6. Jeong J-W, et al. Wireless Optofluidic Systems for Programmable In Vivo Pharmacology and Optogenetics. Cell. 2015; 162:662–674. [PubMed: 26189679]

7. Kim, T-i, et al. Injectable, cellular-scale optoelectronics with applications for wireless optogenetics. Science. 2013; 340:211–216. [PubMed: 23580530]

8. Li W, Kwon KY, Lee H-M, Ghovanloo M, Weber A. Design, Fabrication, and Packaging of an Integrated, Wirelessly-Powered Optrode Array for Optogenetics Application. Frontiers in Systems Neuroscience. 2015; 9

9. Zorzos AN, Scholvin J, Boyden ES, Fonstad CG. Three-dimensional multiwaveguide probe array for light delivery to distributed brain circuits. Opt Lett. 2012; 37:4841–4843. [PubMed: 23202064]

10. Schwaerzle, M., Elmlinger, P., Paul, O., Ruther, P. Micro Electro Mechanical Systems (MEMS); 28th IEEE International Conference on; 2015. p. 162-165.

11. McAlinden N, Gu E, Dawson MD, Sakata S, Mathieson K. Optogenetic activation of neocortical neurons in vivo with a sapphire-based micro-scale LED probe. Frontiers in Neural Circuits. 2015; 9

12. McCall JG, et al. Fabrication and application of flexible, multimodal light-emitting devices for wireless optogenetics. Nat Protocols. 2013; 8:2413–2428. [PubMed: 24202555]

13. Szabo V, Ventalon C, De Sars V, Bradley J, Emiliani V. Spatially selective holographic photoactivation and functional fluorescence imaging in freely behaving mice with a fiberscope. Neuron. 2014; 84:1157–1169. [PubMed: 25433638]

14. Pisanello F, et al. Multipoint-Emitting Optical Fibers for Spatially Addressable In Vivo Optogenetics. Neuron. 2014; 82:1245–1254. [PubMed: 24881834]

15. Pisanello M, et al. Modal demultiplexing properties of tapered and nanostructured optical fibers for in vivo optogenetic control of neural activity. Biomedical Optics Express. 2015; 6:4014–4026. [PubMed: 26504650]

16. Aravanis AM, et al. An optical neural interface: in vivo control of rodent motor cortex with integrated fiberoptic and optogenetic technology. Journal of neural engineering. 2007; 4:S143. [PubMed: 17873414]

17. Yizhar O, Fenno LE, Davidson TJ, Mogri M, Deisseroth K. Optogenetics in neural systems. Neuron. 2011; 71:9–34. [PubMed: 21745635]

18. Stujenske, Joseph M., Spellman, T., Gordon, Joshua A. Modeling the Spatiotemporal Dynamics of Light and Heat Propagation for In Vivo Optogenetics. Cell Reports. 2015; 12:525–534. [PubMed: 26166563]

19. Oldenburg IA, Sabatini BL. Antagonistic but Not Symmetric Regulation of Primary Motor Cortex by Basal Ganglia Direct and Indirect Pathways. Neuron. 2015; 86:1174–1181. [PubMed: 26050037]

20. Greenberg ME, Ziff EB, Greene LA. Stimulation of neuronal acetylcholine receptors induces rapid gene transcription. Science. 1986; 234:80–83. [PubMed: 3749894]

21. Zhao S, et al. Cell type-specific channelrhodopsin-2 transgenic mice for optogenetic dissection of neural circuitry function. Nat Methods. 2011; 8:745–752. [PubMed: 21985008]

22. Wiltschko AB, et al. Mapping Sub-Second Structure in Mouse Behavior. Neuron. 2015; 88:1121–1135. [PubMed: 26687221]

23. Kravitz AV, et al. Regulation of parkinsonian motor behaviours by optogenetic control of basal ganglia circuitry. Nature. 2010; 466:622–626. [PubMed: 20613723]

24. Boyden ES, Zhang F, Bamberg E, Nagel G, Deisseroth K. Millisecond-timescale, genetically targeted optical control of neural activity. Nat Neurosci. 2005; 8:1263–1268. [PubMed: 16116447]

25. Zhang F, et al. Multimodal fast optical interrogation of neural circuitry. Nature. 2007; 446:633–639. [PubMed: 17410168]

26. Klapoetke NC, et al. Independent optical excitation of distinct neural populations. Nat Meth. 2014; 11:338–346.

27. Cardin JA, et al. Targeted optogenetic stimulation and recording of neurons in vivo using cell-type-specific expression of Channelrhodopsin-2. Nat protoc. 2010; 5:247–254. [PubMed: 20134425]

28. Warden MA, Cardin JA, Deisseroth K. Optical-Neural Interfaces in Freely Moving Mammals. Annu Rev Biomed Eng. 2014; 16:103. [PubMed: 25014785]

29. Eshel N, et al. Arithmetic and local circuitry underlying dopamine prediction errors. Nature. 2015; 525:243–246. [PubMed: 26322583]

30. Al-Juboori SI, et al. Light Scattering Properties Vary across Different Regions of the Adult Mouse Brain. PLoS ONE. 2013; 8:e67626. [PubMed: 23874433]

31. Hanks TD, et al. Distinct relationships of parietal and prefrontal cortices to evidence accumulation. Nature. 2015; 520:220–223. [PubMed: 25600270]

32. Stark E, Koos T, Buzsaki G. Diode-probes for spatiotemporal optical control of multiple neurons in freely-moving animals. Journal of Neurophysiology. 2012

33. Gilmartin MR, Miyawaki H, Helmstetter FJ, Diba K. Prefrontal activity links nonoverlapping events in memory. The Journal of neuroscience : the official journal of the Society for Neuroscience. 2013; 33:10910–10914. [PubMed: 23804110]

34. Lambelet P, Sayah A, Pfeffer M, Philipona C, Marquis-Weible F. Chemically etched fiber tips for near-field optical microscopy: a process for smoother tips. Applied optics. 1998; 37:7289–7292. [PubMed: 18301560]

35. McGeorge AJ, Faull RL. The organization of the projection from the cerebral cortex to the striatum in the rat. Neuroscience. 1989; 29:503–537. [PubMed: 2472578]

36. Afraz A, Boyden ES, DiCarlo JJ. Optogenetic and pharmacological suppression of spatial clusters of face neurons reveal their causal role in face gender discrimination. Proc Natl Acad Sci U S A. 2015; 112:6730–6735. [PubMed: 25953336]

37. Lund JS, Boothe RG. Interlaminar connections and pyramidal neuron organisation in the visual cortex, area 17, of the Macaque monkey. The Journal of Comparative Neurology. 1975; 159:305–334.

38. Saleh, BEA., Teich, MC. Fundamentals of photonics. 2nd edn. Wiley Interscience; 2007.

39. Sparta DR, et al. Construction of implantable optical fibers for long-term optogenetic manipulation of neural circuits. Nat Protoc. 2012; 7:12–23.
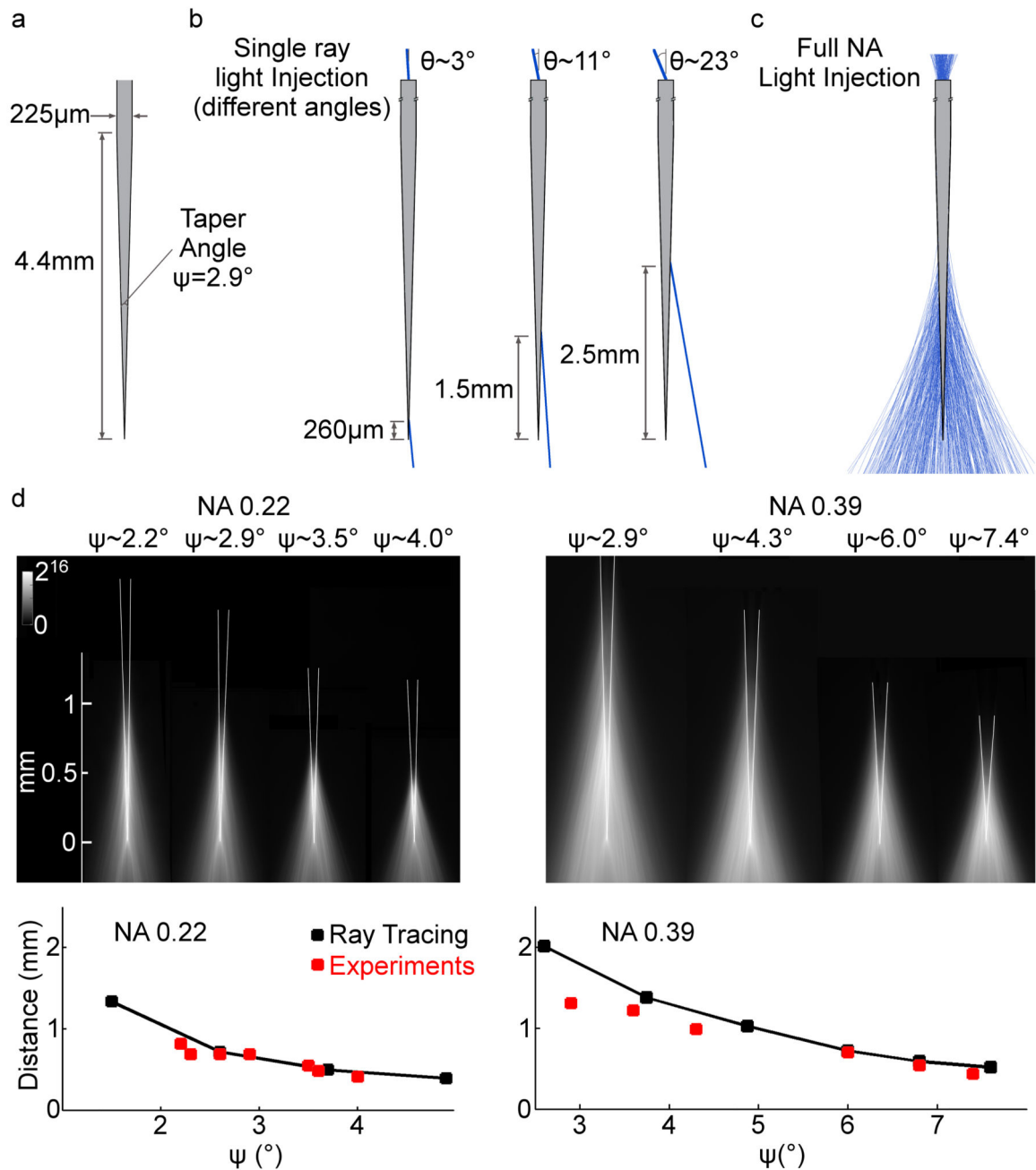
Figure 1. Emission properties of TFs

a, Schematic representation of a typical TF geometry (NA=0.39, taper angle ψ=2.9°, taper length 4.4 mm, core/cladding diameters 200/225 μm).

b, Ray tracing simulations of emission from the taper tip resulting from injecting a single ray in the fiber at different angles.

c, Ray distributions resulting from injecting light using the full NA of the fiber.

d, *top*, Image of fluorescence generated by light emitted from tapered fibers with the specified geometries immersed in a fluorescein solution. *bottom,* The graphs depict

calculated (black) and measured (red) emission lengths (evaluated as the full width at half maximum $L_{0.5}$) for 0.22 NA and 0.39 NA TFs as a function of the taper angle. 0.22 NA TFs have core/cladding diameters of 50/125 μm, whereas 0.39 NA TFs have core/cladding diameters of 200/225 μm.
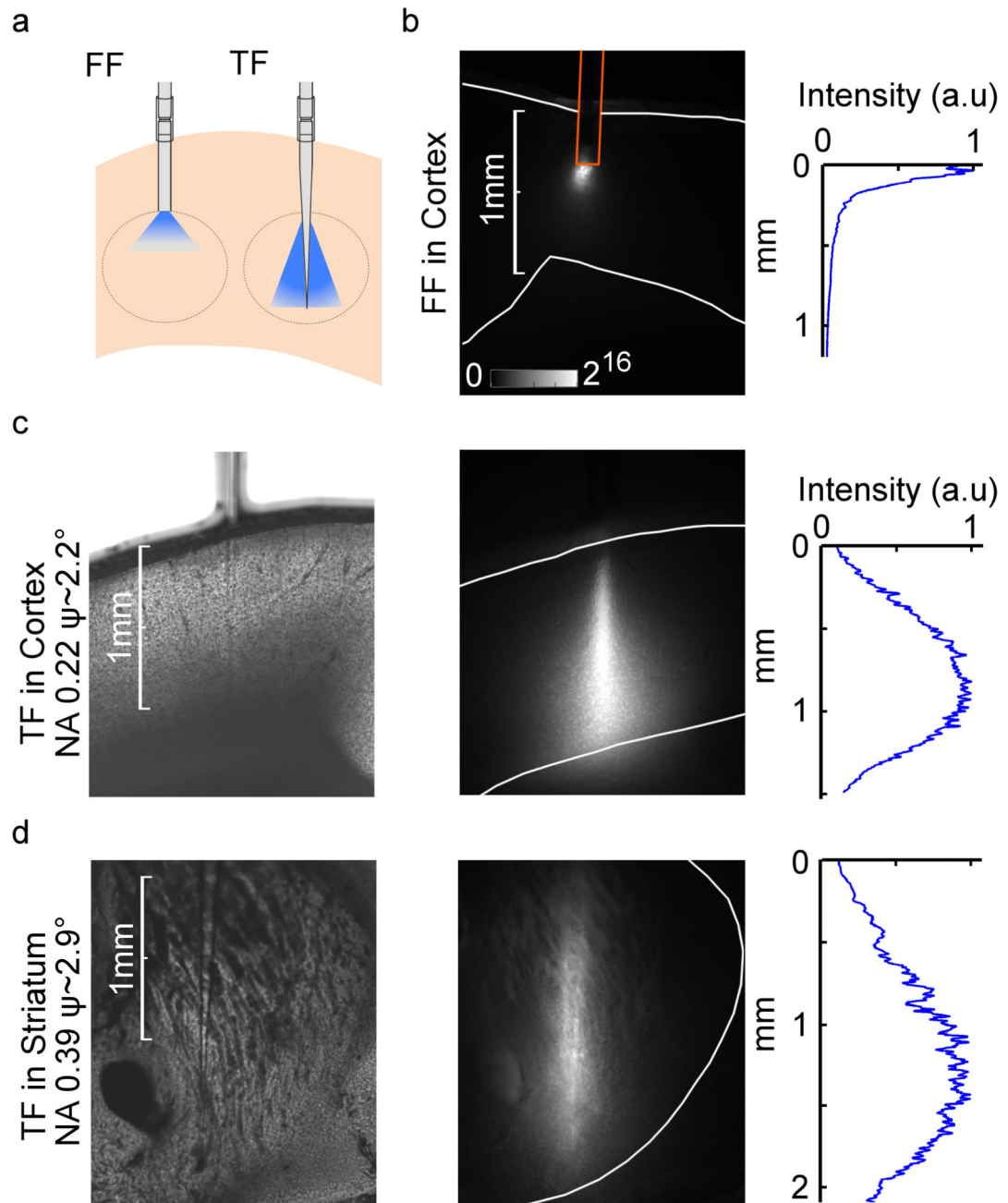
Figure 2. Emission properties of TFs in brain slices

a, Schematic of light delivery in brain tissue through FFs and TFs.

b, *left*, Image of fluorescence induced by light emission from an FF implanted into cortex in a fluorescein impregnated brain slice. Gray scale represents fluorescence intensity in arbitrary units of a linear scale. *right,* Normalized fluorescence intensity profile in the tissue starting from the fiber end face

c and **d**, Bright field images (*left*) to identify the position of the TFs in the fluorescein impregnated cortical or striatal brain slice used for acquisition of the fluorescence images

(*middle*). Gray scale is the same as in (b). *right,* Normalized profiles of fluorescence intensities beside the taper, starting from the first emission point.
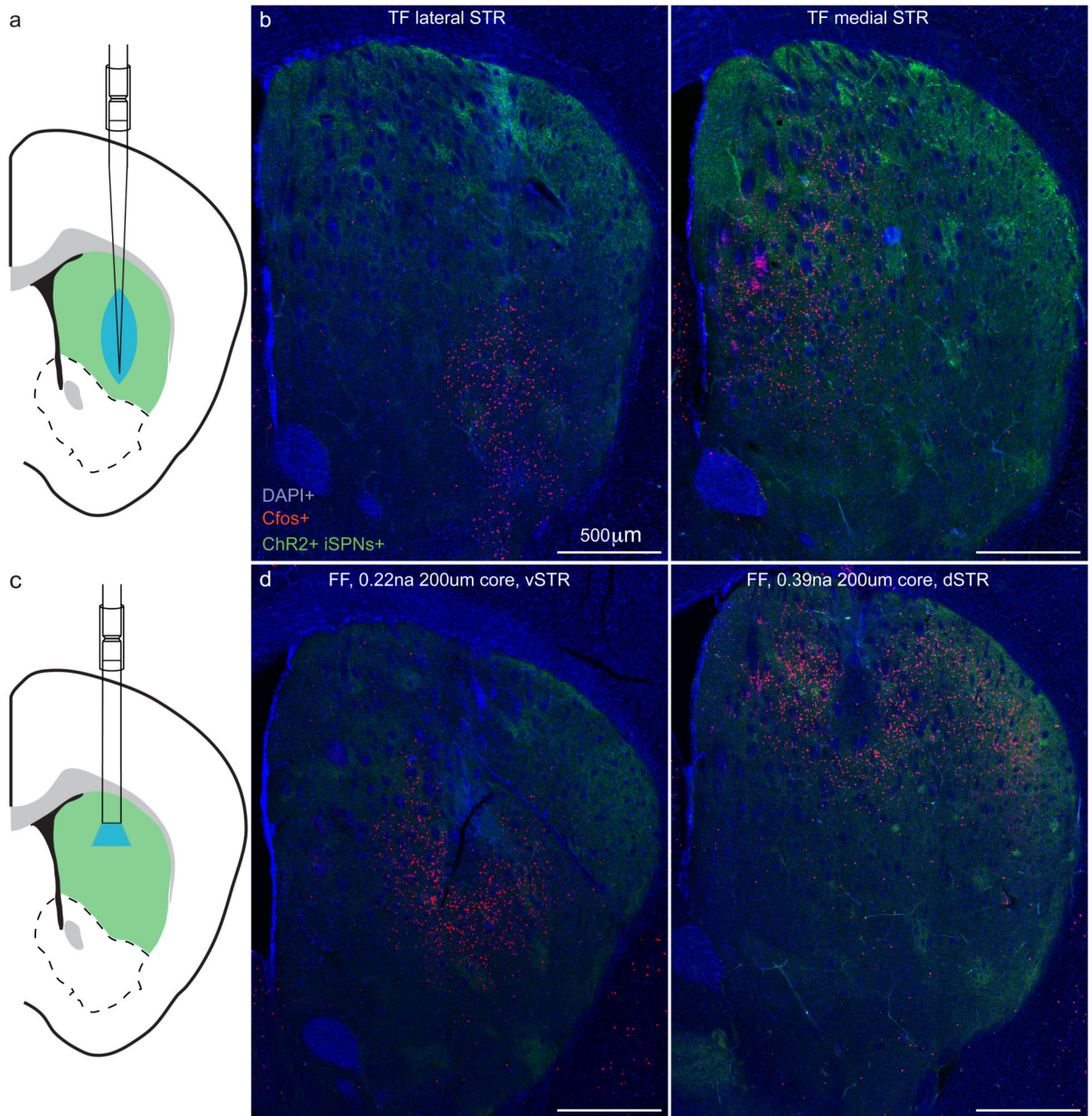
Figure 3. *In vivo* examination of effective excitation in striatum

a, Schematic of experimental preparation showing a TF inserted into the striatum of a mouse expressing ChR2 in indirect pathway SPNs (iSPNs).

b, c-fos expression (red) in the striatum (coronal section, 0.85 mm anterior to Bregma) of an animal expressing ChR2-YFP in iSPNs (green) after light stimulation delivered by a TF in lateral (*left*) or medial (*right*) striatum. DAPI is shown in blue. Representative image of two independent replicates.

c, Schematic of experimental preparation as in (a) showing placement of a flat-faced fiber (FF).

d, As in (b) showing c-fos induction by light delivery from a FF in dorsal (*left,* 0.22 NA) or ventral (*right,* 0.39 NA) striatum. Representative image of two independent replicates.
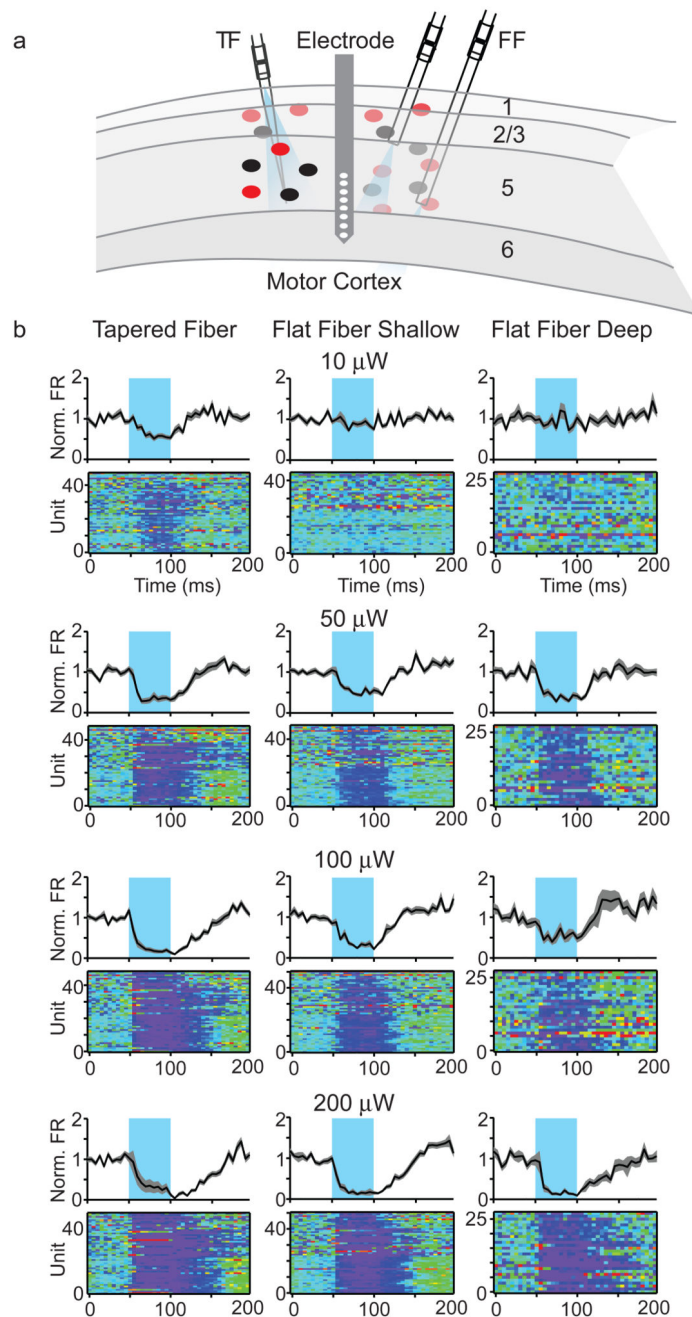
Figure 4. Optogenetic manipulation of motor cortex with TFsc

a, Schematic of the experimental preparation. A 16 channel multi-electrode array is placed in primary motor cortex of a VGAT-ChR2 BAC transgenic mouse and maintained throughout the experiment. Units are recorded throughout cortical layers. A TF or FF in either a shallow or deep position is placed in cortex. The firing rates of individual units are compared during the basal period or during 50 ms optogenetic excitation cortical GABAergic interneurons

b, Average normalized firing rates (black line with shaded area showing SEM) across cells with and without light (*top*) and pseudo-colored representations of normalized across-trial average firing rate of each unit as a function of time (*bottom*). The color scale ("Rainbow" in Igor Pro) indicates relative firing rates of each cell (0=dark blue to 3=red) normalized to its baseline (0-50 ms). The period of light delivery (50 ms) is shown in the cyan shaded regions. Data (n-values 45, 49, 51, 51, 28, 28, 28, 28, 48, 49, 49, and 49 cells) are shown for each fiber configuration (*left:* TF, *middle:* FF shallow, *right:* FF deep) and at 4 power levels (10, 50, 100, and 200 µW total emission from the fiber before implantation in the brain.
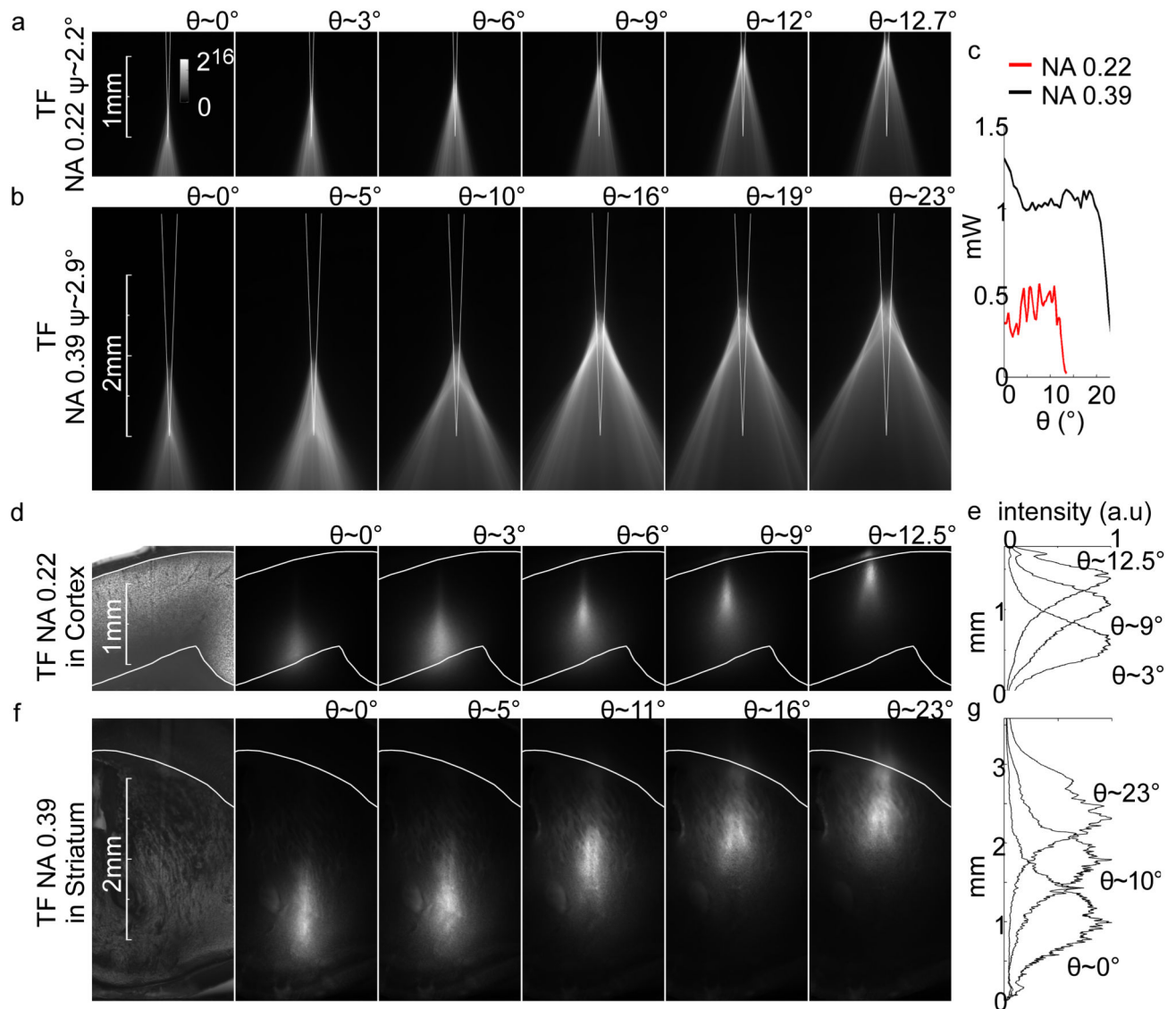
Figure 5. Site selective light delivery with TFs

a, Light delivery geometry for several values of light injection angle θ with a 0.22NA/ψ=2.2° TF into a fluorescein solution. Gray scale represents fluorescence intensity in arbitrary units and is the same for all panels.

b, Light delivery geometry for several values of light injection angle θ with a 0.39 NA/ψ =2.9° TF into a fluorescein solution.

c, Total Output power for a fixed input of 2.25 mW for TFs with 0.22 NA/ψ=2.2° TF (red line) and 0.39 NA/ψ=2.9° TF (black line)

d, Site selective light delivery with a 0.22 NA/ψ=2.2° TF implanted into the cortical region of a fluorescently stained mouse brain slice.

e, Normalized fluorescence intensity profiles, measured beside the taper, from the fluorescence images in (d).

f, Site selective light delivery with a 0.39NA/ ψ=2.9° TF implanted into the striatum of a fluorescently stained mouse brain slice.

g, Normalized fluorescence intensity profiles, measured beside the taper, from the fluorescence images in (f).
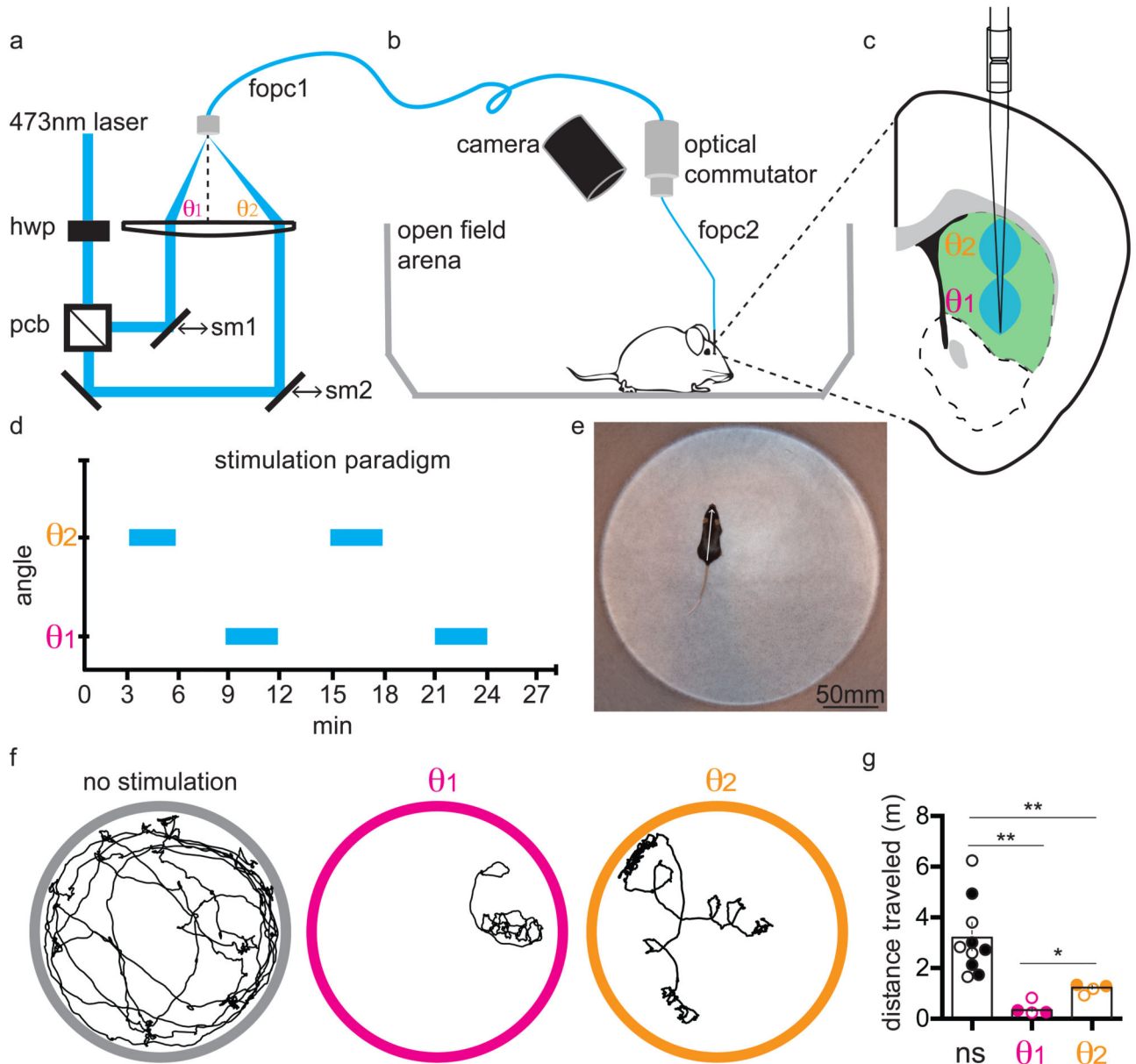
Figure 6. Selective light delivery with TFs in the open field

a, Schematic of optical setup. The output of a polarized laser was passed through a ½-wave plate (hwp) to rotate the polarization before entering a polarizing beam cube (pbc) that transmits and reflects, respectively, horizontally and vertically polarized light. Rotation of the hwp determines the fraction of laser light entering each path. Each of the laser paths is directed to a 2-inch collection lens via a sliding mirror (sm1 and sm2) that can be moved linearly to determine the launch angle into the first fiber-optic patch cord (fopc1).
b, Fiber optic patch cable (fopc1) was connected from the optical pathway shown in (a) to a commercial optical commutator from which a second fiber optic patch cable (fopc2) led to

the TF implanted in the animal. A camera above the arena monitored the location and depth of the mouse.

c, The TF was implanted in the striatum (0.85A, 1.4L, 4.1D) of a transgenic animal expressing ChR2-YFP in iSPNs to allow for stimulation of two regions of striatum. Light input at θ1 (*magenta*) and θ2 (*orange*) angles resulted in emission that targeted the ventral and dorsal striatum, respectively.

d, Example of stimulation paradigm in the open field arena on day 1. Animals spent a total of 27 min in the open field with 3 min sessions of either no light, light on at angle θ1, or light on angle at θ2. On a subsequent day of analysis the order of θ_1 and θ_2 stimulation were reversed.

e, Snapshot of a mouse in the open field with an overlaid vector highlighting the simple feature extraction of position and orientation.

f, Example of the positions of one mouse during 3-minute session of no stimulation (*left*), ventral stimulation (θ_1, *middle*), and dorsal stimulation (θ_2, *right*).

g, Quantification of distance traveled in the 3 conditions for the example mouse shown in (f). Significant differences were observed between the no stimulation (*left*), ventral stimulation (*middle*) and the dorsal stimulation (*right*) conditions. Bars indicate the means of all data points from individual 3 min blocks, which are shown by the circles (not filled: day 1; filled: day 2). *p = 0.028, **p=0.002, using a two-tailed Mann-Whitney U test.
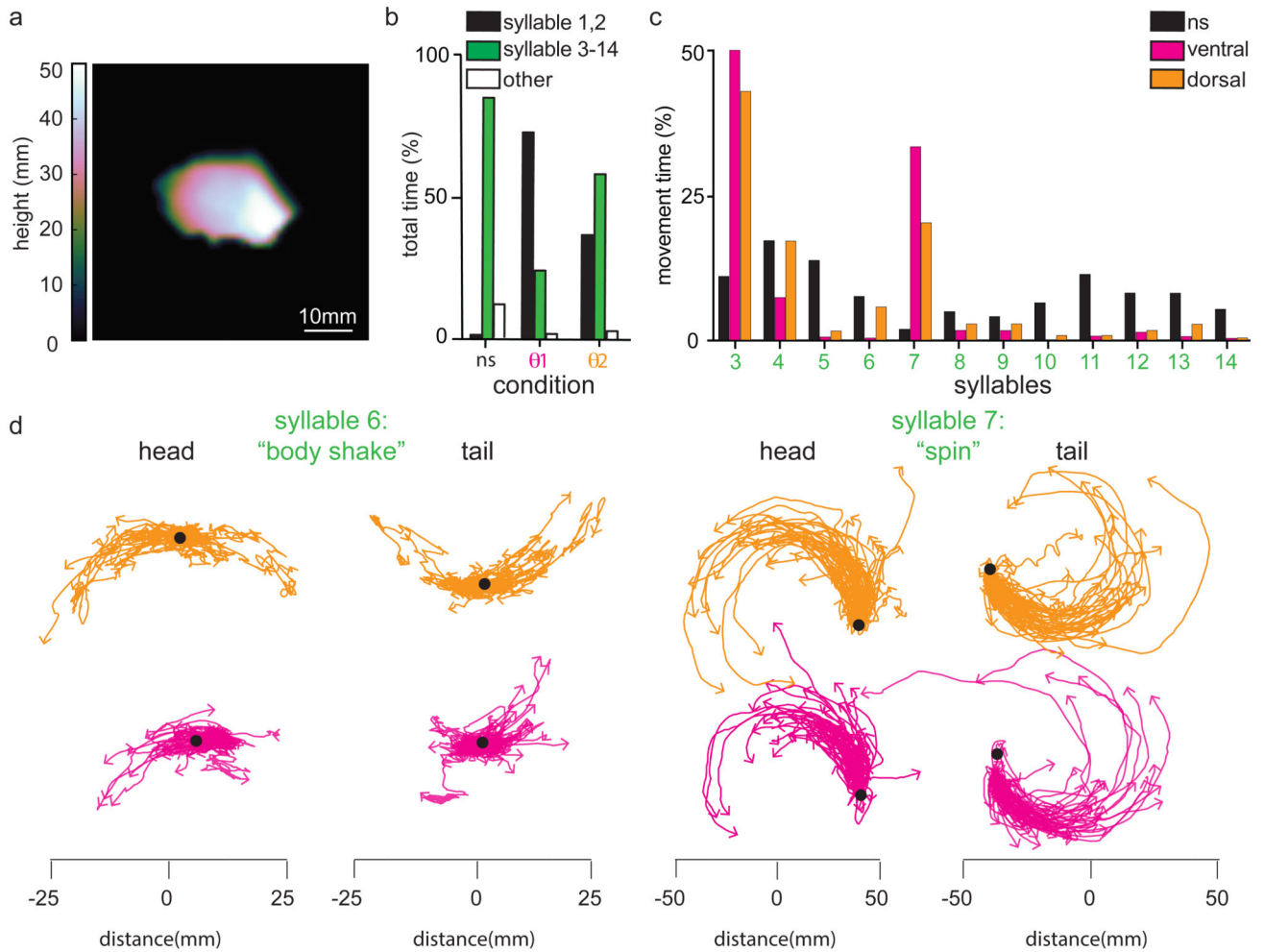
Figure 7. Mapping sub-second structure of behavior during optogenetic manipulation of ventral or dorsal striatum

a, Snapshot of a mouse in the open field with the height of the body at each pixel indicated by the color scale.

b, The percent total behavior data (same mouse as in Figure 6) explained in each condition (ns, θ_1, and θ_2 stimulation) by the major pause related (*black*) syllables (1 and 2), the major movement-related (*green*) syllables (3-14) and all other syllables (*white*).

c, Percent expression of the dominant non-pause, i.e. movement related, syllables (3-14), showing differential expression of syllables across stimulation conditions.

d, The trajectories of the head and tail of the mouse relative to its body center for syllable 6 (*left*) and syllable 7 (*right*) in either the ventral (θ_1, *magenta*) and dorsal (θ_2, *orange*) stimulation conditions. The black dots depict the starting point of each of the aligned trajectories of the head and tail. All (limited to 100) instances of the trajectories of the head and tail relative to its body center are shown.